© 2020. Published by The Company of Biologists Ltd | Journal of Cell Science (2020) 133, jcs241216. doi:10.1242/jcs.241216

RESEARCH ARTICLE

The microtubule end-binding affinity of EB1 is enhanced by a dimeric organization that is susceptible to phosphorylation

Yinlong Song[1], Yikan Zhang[2], Ying Pan[1,2], Jianfeng He[1], Yan Wang[2], Wei Chen[1], Jing Guo[3], Haiteng Deng[3], Yi Xue[1,2,*], Xianyang Fang[2,*] and Xin Liang[1,*]

ABSTRACT

In cells, microtubule dynamics are regulated by plus-end tracking proteins (+TIPs). End-binding protein 1 (EB1, also known as MAPRE1) acts as a master regulator of +TIP networks by targeting the growing ends of microtubules and recruiting other factors. However, the molecular mechanism underlying high-affinity binding of EB1 to microtubule ends remains an open area of research. Using single-molecule imaging, we show that the end-binding kinetics of EB1 change when the polymerization and hydrolysis rates of tubulin dimers are altered, confirming that EB1 binds to GTP–tubulin and/or GDP–P_i–tubulin at microtubule growing ends. The affinity of wild-type EB1 to these sites is higher than that of monomeric EB1 mutants, suggesting that both calponin homology domains present in the EB1 dimer contribute to end binding. Introduction of phosphomimetic mutations into the EB1 linker domain weakens the end-binding affinity and confers a more curved conformation on the EB1 dimer without compromising dimerization, suggesting that the overall architecture of EB1 is important for its end-binding affinity. Taken together, our results provide insights into how the high-affinity end-binding of EB1 is achieved and how this activity may be regulated in cells.

KEY WORDS: EB1, Microtubule, Tip-tracking, Single-molecule imaging, Microtubule-associated protein

INTRODUCTION

In cells, the regulation of microtubule dynamics plays a key role in cell division, polarization and motility, and involves a large number of proteins (Bowne-Anderson et al., 2015). Notable among such proteins is a complex network of molecules that regulates the dynamics of microtubule growing ends (Akhmanova and Steinmetz, 2008). These proteins are termed plus-end tracking proteins (+TIPs). End-binding family proteins, including end-binding protein 1 (EB1, also known as MAPRE1), act as core components of +TIP networks, specifically recognizing the growing end of microtubules and recruiting other +TIPs (Galjart, 2010). The high end-binding affinity of EB1 is key for the function of the protein and, in turn, for the dynamics of +TIPs.

How does EB1 bind to microtubule growing ends? Two possible mechanisms have been proposed. Microtubules, which provide binding sites for EB1, grow by the addition of free GTP–tubulin dimers to the growing end. The temporal delay between microtubule formation and GTP hydrolysis leads to the creation of a region at the growing end of microtubules that is rich in GTP–tubulin and GDP–P_i–tubulin, termed the GTP cap (Howard, 2001). Because EB1 binding favors GTPγS- and GMPCPP-bound microtubules (comprising analogues of GTP–tubulin or GDP–P_i–tubulin) over GDP-bound microtubules (Maurer et al., 2011, 2012; Zanic et al., 2009), it is thought that the GTP cap provides high-affinity binding sites for EB1. An additional mechanism for EB1 binding to microtubule growing ends was indicated by the recent discovery that EB1 also preferentially binds to open microtubule structures, suggesting that the structure of the tapered end of growing microtubules facilitates the binding of EB1 (Reid et al., 2019). Because the GTP cap and the tapered microtubule tip are dynamic structures (Duellberg et al., 2016; Gardner et al., 2011), a predicted consequence of both mechanisms is that the end-binding kinetics of EB1 might change along with changes to microtubule dynamics, for example at different growth rates.

How does the structure of EB1 support the high-affinity end-binding activity of the protein? EB1 is a homodimer and binds to microtubules in a non-cooperative manner (Maurer et al., 2011). Comparative observations of the fluorescence intensity of EB1 and monomeric kinesin motor domain (both tagged with GFP) on stabilized microtubules at saturating concentrations suggested that EB1 binds to microtubules with one of its two calponin homology (CH) domains per tubulin dimer (Maurer et al., 2011). Additionally, although monomeric EB1 retains a preference for microtubule growing ends, it shows a reduced comet signal (Komarova et al., 2009; Maurer et al., 2011). These results suggest that dimerization contributes to the high end-binding affinity of EB1. EB1 dimerizes via the C-terminal coiled-coil domain of the protein, which is linked to the CH domain via a linker domain in each monomer. Because the linker domain is predicted to lack regular secondary structure (Buey et al., 2011), it is thought to be disordered, and thereby the two CH domains are probably independent. However, chemical cross-linking experiments show that the two CH domains of a single EB1 dimer can connect to each other and interact with the linker domain, suggesting that the two EB1 monomers in the dimer are structurally constrained and that the linker domain is folded to some extent (Buey et al., 2011). How does such a structural organization contribute to the high end-binding affinity of EB1? Direct biochemical data are lacking.

How is the overall structure of EB1 organized? Previous studies show that EB1, despite being a homodimer, has an asymmetric structure (Buey et al., 2011). The linker domain is thought to be key in establishing the structural asymmetry. This domain has an evolutionarily divergent sequence, within which there are multiple positively charged residues. Mutating these residues decreases the microtubule end-binding activity of EB1 (Xia et al., 2014). The

[1]Tsinghua-Peking Joint Center for Life Sciences, School of Life Sciences, Tsinghua University, 100084 Beijing, China. [2]Beijing Advanced Innovation Center for Structural Biology, School of Life Sciences, Tsinghua University, 100084 Beijing, China. [3]Protein Chemistry Facility at the Center for Biomedical Analysis of Tsinghua University, 100084 Beijing, China.

*Authors for correspondence (xinliang@tsinghua.edu.cn; yixue@mail.tsinghua.edu.cn; fangxy@tsinghua.edu.cn)

X.L., 0000-0001-7915-8094

Received 4 November 2019; Accepted 28 February 2020

Journal of Cell Science (2020) 133, jcs241216. doi:10.1242/jcs.241216

linker domain also contains several potential phosphorylation sites, some of which are known to be the substrate of cytoplasmic kinases, such as ASK1 (also known as MAP3K5) and, in budding yeast, the Aurora kinase Ipl1p (Luo et al., 2016; Zimniak et al., 2009). Phosphorylation of these sites alters the end-binding activity of EB1 during several cellular processes, including correction of improper microtubule attachment to the kinetochore (Zimniak et al., 2009) and control of spindle orientation (Luo et al., 2016), thereby serving as an important mechanism for regulation of EB1 function. These observations led to the hypothesis that the linker domain helps organize the overall architecture of EB1 and can serve as a target for cellular regulation (through, for example, its phosphorylation). This hypothesis remains to be further tested in the context of understanding the role of the linker domain in regulation of EB1 end-binding activity.

In this study, we address these questions using *in vitro* reconstituted microtubule end-binding assays and structural analysis (Gell et al., 2010). We demonstrate that the end-binding kinetics of EB1 change along with the growth velocity of microtubules and the hydrolysis rate of tubulins at microtubule growing ends, providing *in vitro* evidence for a high-affinity interaction between EB1 and the GTP cap. The end-binding affinity of wild-type EB1 at the single-molecule level is much higher than the end-binding affinity of monomeric EB1 mutants, suggesting that both monomers in the EB1 dimer bind to the growing end of microtubules and contribute to the high end-binding affinity. Further analyses show that introduction of phosphomimetic mutations to the linker domain leads to a reduction in the end-binding affinity of EB1 to the level of affinity shown by EB1 monomers, and causes EB1 to adopt a more curved conformation without compromising the dimeric organization. These results support the idea that the overall structure of EB1 facilitates end-binding activity, and that the linker domain is structurally important for adoption of such an architecture. Taken together, our findings provide further insights into the mechanism of EB1 binding to microtubules and how this binding activity can be regulated in cells.

RESULTS

Single-molecule binding kinetics of EB1 at the growing ends of microtubules

We began by characterizing the single-molecule binding events of wild-type human EB1 at the plus end of growing microtubules (using a tubulin concentration of 20 µM). In our assay, individual end-binding events can be observed (Fig. 1A-C) in the presence of 5 nM EB1–GFP (His-tag removed, Fig. S1). By analyzing the intensity of these events, we confirmed that they represent the

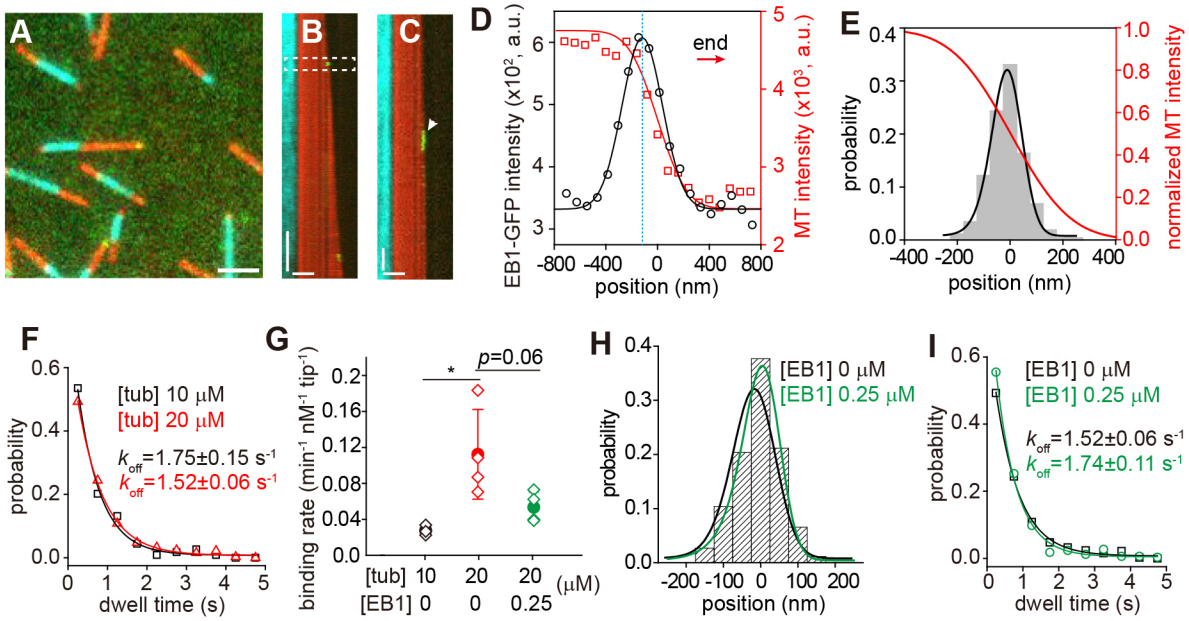

Fig. 1. Single-molecule binding kinetics of EB1 at microtubule growing ends. (A) Representative TIRF image of the *in vitro* microtubule dynamics assay. TAMRA-labeled dynamic microtubules (red), Alexa Fluor 647-labeled GMPCPP seeds (cyan) and EB1–GFP (5 nM; green) are shown. Scale bar: 2 µm. (B) Representative kymograph of a growing microtubule with EB1 molecules at its growing end. The region in the dashed box is enlarged in C. Vertical bar: 100 s. Horizontal bar: 2 µm. (C) The enlarged region from B, showing a representative end-binding event of EB1–GFP (white arrowhead). Vertical bar: 2.5 s. Horizontal bar: 2 µm. (D) Representative intensity profiles of a microtubule end (red) and an EB1–GFP binding event (black). A Gaussian function was used to fit the intensity profile of EB1–GFP and its peak position recorded as the location of the EB1–GFP binding event (blue dotted line). Arrow indicates the direction of the microtubule growing end. (E) The spatial distribution of EB1–GFP (n=264 events) along the longitudinal axis of microtubules. The histogram was fitted to an exponentially modified Gaussian function. The averaged intensity profile of microtubule ends (red line) was used as the positional reference. (F) The probability distributions of the dwell time of single EB1–GFP molecules at two tubulin concentrations (Black: 10 µM tubulin, n=111 events in total from 3 assays. Red: 20 µM tubulin, n=463 events in total from 4 assays). The data were fitted to a single exponential function to calculate the dissociation rates (k_{off}). (G) The apparent association rates of EB1–GFP in various conditions. Black: 10 µM tubulin without non-GFP-tagged EB1, n=198 microtubules in total from 3 assays. Red: 20 µM tubulin without non-GFP-tagged EB1, n=227 microtubules in total from 4 assays. Green: 20 µM tubulin and 0.25 µM non-GFP-tagged EB1, n=232 microtubules in total from 4 assays. Open symbols show means of independent assays, closed symbols show mean±s.d. of all assays. *P<0.05, two-tailed Student's t-test. (H) The spatial distribution of EB1–GFP binding events along the longitudinal axis of microtubules in the presence of 0.25 µM non-GFP-tagged EB1 (n=260 events). The histogram was fitted to an exponentially modified Gaussian function (green line). The black line shows the spatial distribution of EB1–GFP binding events without non-GFP-tagged EB1 (as shown in E). (I) The probability distributions of the dwell time of single EB1–GFP molecules in the absence (black, n=463 events in total from 4 assays) or presence (green, n=337 events in total from 3 assays) of 0.25 µM non-GFP-tagged EB1. The data were fitted to a single exponential function to calculate the dissociation rates (k_{off}). In B, E, H and I, the tubulin concentration used in the experiments is 20 µM.

Journal of Cell Science

Journal of Cell Science (2020) 133, jcs241216. doi:10.1242/jcs.241216

binding of individual EB1 dimers (Fig. S1). To map the spatial distribution of EB1 binding sites at microtubule growing ends, EB1 binding events were recorded at single-molecule level and their precise locations were determined by fitting a Gaussian function to the intensity profile of individual events (Fig. 1D). Using the position of microtubule ends as the reference (i.e. the origin), we overlaid the positions of 264 individual binding events (Fig. 1E). The spatial distribution of these binding events could be well fitted to an exponentially modified Gaussian function, which resembled the shape of the fluorescence profile of an EB1 comet. The length of the EB1 binding region in this condition was 136 nm (FWHM: full width at half maximum), which led us to estimate that the average lifetime [calculated as the ratio of the length of the binding region to the microtubule growth velocity (1.25 µm min^{-1})] of EB1 binding sites was 6.5 s, similar to those reported in earlier studies (Dixit et al., 2009; Maurer et al., 2014).

Having confirmed that the single-molecule EB1 binding events are at the microtubule growing ends, we measured their binding kinetics and addressed how the end-binding kinetics change with microtubule growth velocity and hydrolysis rate. To do this, two parameters were measured. First, the number of binding events per microtubule tip per min per nanomole of EB1–GFP was defined as the macroscopic association rate (k_{on}). Because EB1 binds to microtubules in a non-cooperative manner (Maurer et al., 2011), k_{on} is determined by the microscopic association rate of EB1 on each binding site and the number of such sites per microtubule tip. Second, the macroscopic dissociation rate of EB1 (k_{off}) was defined as the reciprocal of the time constant obtained by fitting a single exponential function to the probability density distribution of the dwell time of individual EB1–GFP molecules. Intuitively, k_{off} should be determined by the microscopic dissociation rate of EB1 from its binding site.

We first measured k_{on} and k_{off} of EB1–GFP at two tubulin concentrations (10 and 20 µM). The corresponding microtubule growth rates were 0.55±0.07 µm min^{-1} [10 µM tubulin, mean±s.d. (unless otherwise stated), n=3 assays (74 microtubules)] and 1.25±0.08 µm min^{-1} [20 µM tubulin, n=3 assays (62 microtubules)]. In these two conditions, EB1–GFP showed an almost unchanged k_{off} [10 µM tubulin, 1.75±0.15 s^{-1}, n=3 assays (111 events); 20 µM tubulin. 1.52±0.06 s^{-1}, n=4 assays (463 events)] (Fig. 1F), but showed an increased k_{on} [10 µM tubulin, 0.03±0.01 min^{-1} nM^{-1} tip^{-1}, n=3 assays (198 microtubules); 20 µM tubulin, 0.11±0.05 min^{-1} nM^{-1} tip^{-1}, n=4 assays (227 microtubules)] when microtubules grew faster (Fig. 1G). Because faster microtubule growth is not expected to change the microscopic affinity of EB1–GFP to its binding site, the observed increase in k_{on} suggests that more EB binding sites are transiently created at microtubule growing ends that have a higher growth rate. This is consistent with the previously described finding that the length of the stabilizing GTP cap increases when microtubules grow faster (Duellberg et al., 2016).

We then measured k_{on} and k_{off} of EB1–GFP in the presence of additional 0.25 µM non-GFP-tagged EB1, which promotes GTP hydrolysis and microtubule catastrophe (Bowne-Anderson et al., 2013), in order to examine the effect of GTP hydrolysis rate on the binding kinetics. The additional non-tagged EB1 only slightly increased the growth rate of microtubules from 1.25±0.08 µm min^{-1} [n=3 assays (62 microtubules)] to 1.39±0.08 µm min^{-1} [n=3 assays (63 microtubules); P<0.05, two-tailed Student's t-test]. Under these conditions, a slightly lower k_{on} [0.05±0.02 min^{-1} nM^{-1} tip^{-1}, n=4 assays (232 microtubules)] was observed in the presence of additional EB1 (Fig. 1G), suggesting a small reduction in the number of EB1 binding sites. To confirm this observation, we measured the length of the EB1 binding region under the same conditions. The spatial distribution of EB1 binding sites shifted towards the growing tip of microtubules and had a reduced width (FWHM=121 nm) (Fig. 1H). Therefore, the lifetime of EB1 binding sites was shorter (5.2 s, a 20% reduction). These observations were consistent with the idea that faster GTP hydrolysis increases the maturation rate of the stabilizing cap and thereby leads to a reduction in the number of EB1 binding sites. Conversely, the k_{off} of individual EB1 binding events did not show a significant change (Fig. 1I), suggesting that the microscopic end-dissociation rate of EB1–GFP is largely independent of the lifetime of EB1 binding sites.

Taken together, our observations show that microtubules with a faster growth rate tend to have more EB1 binding sites, whereas microtubules with a faster GTP hydrolysis rate tend to have fewer and shorter-lived EB1 binding sites. Furthermore, the dissociation rate of EB1 from its binding sites is a more robust parameter that does not substantially vary with changing microtubule growth velocity and hydrolysis rate. This is consistent with the observation that the dwell time of individual EB1 dimers (0.66 s) is much shorter than the lifetime of EB1 binding sites (6.5 s), and with the idea that the slow transition from GTP–tubulin to GDP–tubulin at the growing ends of microtubules is detected by multiple rounds of EB1 binding (Dixit et al., 2009).

Dimerization contributes to the high end-binding affinity of EB1

We next examined how the dimeric organization of EB1 contributes to its end-binding affinity by comparing the single-molecule binding kinetics of wild-type EB1–GFP with $EB1_{143}$–GFP, which consists of a single EB1 CH domain (the domain responsible for microtubule binding) and lacks the linker and coiled-coil domains (Fig. 2A). The k_{on} of $EB1_{143}$–GFP was one-tenth of the k_{on} of wild-type EB1–GFP [$EB1_{143}$–GFP, 0.01±0.003 min^{-1} nM^{-1} tip^{-1}, n=3 assays (151 microtubules); EB1–GFP, 0.10±0.04 min^{-1} nM^{-1} tip^{-1}, n=4 assays (407 microtubules); P<0.01] (Fig. 2B and C). $EB1_{143}$–GFP had a much shorter dwell time than wild-type EB1–GFP (Fig. 2D) and thereby showed a substantially greater k_{off} (3- to 4-fold). The cumulative probability distribution of dwell time suggested that wild-type EB1–GFP molecules are less likely to dissociate from microtubules (Fig. 2E). We also calculated the dissociation probability (P_o) at a specific dwell time (t, taking 0.3 s as an example here), i.e. the ratio of the number of dissociation events observed at 0.3 s to the total number of binding events whose dwell time reached 0.3 s. The P_o of wild-type EB1–GFP was 0.15, lower than that of $EB1_{143}$–GFP (0.53), confirming that binding of wild-type EB1–GFP to microtubules is more stable than $EB1_{143}$–GFP binding to microtubules. Furthermore, if the two EB1 monomers in the dimer independently dissociated from microtubule ends, each with their own P_o, the probability of both CH domains dissociating would be 0.28 (i.e. the square of P_o), still higher than the P_o of wild-type EB1–GFP. The longer dwell time of dimers at molecular level could be explained by the reattachment mechanism suggested in a previous study (Feng et al., 2018). Using the equation developed by Feng et al. (2018) for calculating the reattachment rate of a monomer within a dimer:

$$k_{reatt} = \frac{2}{t_1} \times \frac{(t_2 - t_1)}{t_1},$$

where k_{reatt} is reattachment rate, t_1 is the dwell time of a monomer and t_2 is the dwell time of a dimer, we calculated the k_{reatt} of EB1–GFP in the dimer to be 34 s^{-1}. This reattachment rate is much faster than the

Journal of Cell Science (2020) 133, jcs241216. doi:10.1242/jcs.241216

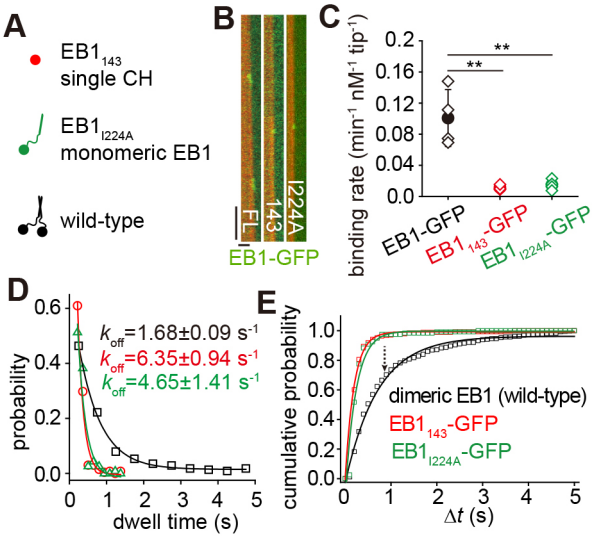

Fig. 2. Comparison between the end-binding kinetics of $EB1_{143}$–GFP, $EB1_{I224A}$–GFP and wild-type EB1–GFP. (A) Schematics of $EB1_{143}$–GFP (red), $EB1_{I224A}$–GFP (green) and wild-type EB1–GFP (black). The color-coding of EB1 variants used here is also used in C–E. (B) Representative kymographs showing individual end-binding events of $EB1_{143}$–GFP, $EB1_{I224A}$–GFP and EB1–GFP (concentration of EB1–GFP and mutants, 5 nM; tubulin concentration, 14 µM). Red: dynamic microtubule. Green: wild-type (full length, FL) or monomeric mutant EB1–GFP. Vertical bar: 5 s. Horizontal bar: 2 µm. (C) The apparent association rates of $EB1_{143}$–GFP (n=151 microtubules in total from 3 assays), $EB1_{I224A}$–GFP (n=284 microtubules in total from 4 assays) and EB1–GFP (n=407 microtubules in total from 4 assays). Open symbols show means of independent assays, closed symbols show mean± s.d. of all assays. **P<0.01, two-tailed Student's t-test. Note that all three EB1 variants at the working concentration (5 nM) have negligible effects on microtubule growth rate. (D) The probability distributions of the dwell time of single $EB1_{143}$–GFP (n=269 events in total from 3 assays), $EB1_{I224A}$–GFP (n=120 events in total from 4 assays) and EB1–GFP (n=427 events in total from 4 assays). The data were fitted to a single exponential function to calculate the dissociation rates (k_{off}). (E) The cumulative probability distributions of the dwell time of $EB1_{143}$–GFP, $EB1_{I224A}$–GFP and wild-type EB1 after a given period of time (Δt). The dashed arrow indicates the reduction in dissociation probability for dimeric EB1.

dissociation rate of a monomer and thereby suggests that the longer bound duration involves multiple cycles of detachment and attachment of the two monomers while the dimer remains bound on microtubules. Based on these results, we conclude that the two EB1 monomers in the dimer both contribute to the high end-binding affinity.

To further address whether the positively charged linker domain directly increases the affinity of the CH domain to the negatively charged surface of microtubules, we studied $EB1_{I224A}$–GFP, a monomeric mutant of full-length EB1 (Slep et al., 2005). Both the k_{on} and k_{off} of $EB1_{I224A}$–GFP were close to those of $EB1_{143}$–GFP (Fig. 2C,D), suggesting that the monomeric linker domain does not significantly change the binding affinity of the CH domain to microtubule growing ends.

What could be the structural basis for the high end-binding affinity of EB1? Two possible mechanisms were considered. The spacing between adjacent EB1 binding sites on a microtubule lattice is either 8 nm (longitudinal) or 6 nm (circumferential), so it is possible that the overall architecture of EB1 dimer facilitates or stabilizes the binding of the two CH domains. The linker domain is thought to be important for the overall architecture of EB1, so it might play an indirect role in enhancing the end-binding affinity by organizing the two monomers. Alternatively, the two linker domains within the dimer, despite having no significant contribution to the binding affinity of monomers, could promote end binding in a more direct way, for example, through electrostatic interaction with the negatively charged surface of microtubules.

Phosphomimetic mutations in the linker domain reduce the end-binding affinity of EB1

To further understand the aforementioned candidate mechanisms, we examined how the linker domain contributes to the end-binding affinity and the overall structure of EB1. Previous studies showed that phosphorylation of serine and threonine residues in the linker domain by the budding yeast Aurora kinase Ipl1p reduces the comet signal of an EB family member (Zimniak et al., 2009). Such phosphorylations provide an opportunity to study the role of the linker domain by making minimal structural modifications that are also relevant to the cellular regulation of EB1. In our experiments, we studied phosphomimetic mutants, instead of *in vitro* phosphorylated EB1, for two reasons. Firstly, the phosphomimetic mutants can recapitulate the behavior of phosphorylated EB1 in cells (Zimniak et al., 2009). Secondly, the use of phosphomimetic mutations facilitates the purification of a more homogeneous population of modified proteins, which is critical for our single-molecule analysis.

We purified four phosphomimetic mutants of EB1–GFP (4D–GFP, 2D–GFP, S155D–GFP and T166D–GFP) (Fig. 3A and Fig. S2) with all mutations located in the linker domain. These mutation sites were chosen as they are the substrates of known kinases (Nehlig et al., 2017). The end-binding comet signal was robust in the case of wild-type EB1–GFP, but varied in appearance with the EB1 mutants (Fig. 3B). To quantify the end-binding signal of EB1 and the phosphomimetic mutants, we averaged the comet signals from 120 consecutive frames of a growing microtubule (Fig. 3C) and measured the integrated intensity of comet signals (Fig. 3D) (Maurer et al., 2014). This showed that 4D–GFP had the weakest comet signal, being ∼40% of the wild-type EB1-GFP signal (Fig. 3E). The comet signals of the 2D–GFP, S155D–GFP and T166D–GFP mutants appeared to be statistically indistinguishable from the EB1–GFP signal (Fig. 3E). However, we noted that the accuracy of this measurement can be interfered with by small EB1–GFP aggregates observed to sometimes form at the salt (50 mM KCl) and protein concentrations (200 nM) used in this set of experiments. Therefore, we further measured the single-molecule binding kinetics at a lower protein concentration (5 nM) but a higher salt condition (100 mM KCl). We found that 4D–GFP, 2D–GFP and S155D–GFP all showed a reduced k_{on}, whereas the k_{on} of T166D–GFP was statistically indistinguishable from that of wild-type EB1–GFP (Fig. 3F). Furthermore, 4D–GFP and 2D–GFP, but not the two single-site mutants, showed an increased k_{off} (Fig. 3G). Therefore, the mutations of the linker domain reduce the end-binding affinity of EB1–GFP with the extent of change appearing to increase with the number of mutations. Furthermore, the cumulative probability distributions of dwell time showed that 4D–GFP had a similar dissociation probability to that of the monomeric EB1–GFP mutant (Fig. 3H). This result is surprising because phosphorylation of the linker domain is not expected to disrupt the dimerization of EB1.

We then measured the effects of the EB1 mutants on microtubule dynamics. As a control, EB1–GFP (200 nM) slightly increased microtubule growth rate and significantly enhanced catastrophe frequency (Fig. S2). By comparison, the four mutants had weaker effects on microtubule dynamics, especially on catastrophe frequency (Fig. S2). In addition, we noted that 200 nM 4D–GFP and 50 nM EB1–GFP showed similar end-binding signals and had similar effects on microtubule dynamics (Fig. S3), demonstrating

Journal of Cell Science (2020) 133, jcs241216. doi:10.1242/jcs.241216

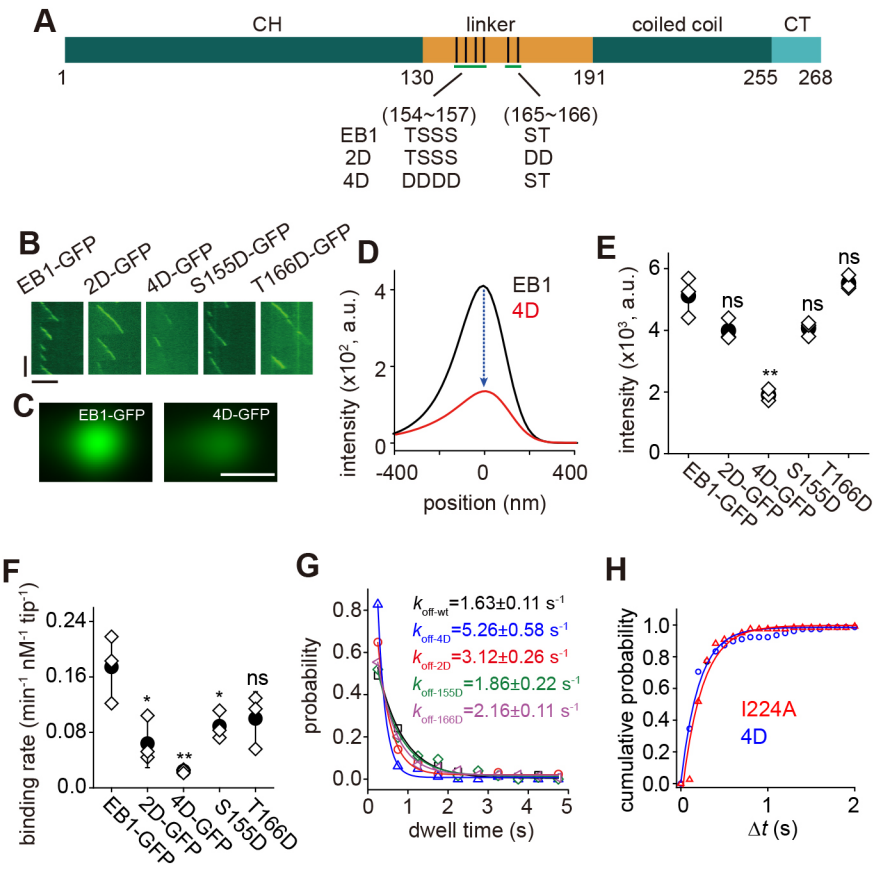

Fig. 3. Phosphomimetic mutations in the linker domain reduce the end-binding affinity of EB1 mutants. (A) Schematic showing the protein domains of EB1 and the sites of phosphomimetic mutations (CT, carboxyl-terminal domain). (B) Representative kymographs showing the comet signals of EB1 and the phosphomimetic mutants. Vertical bar: 2 min. Horizontal bar: 5 µm. Tubulin: 20 µM. Wild-type and mutant EB1: 200 nM. (C) Averaged comet images (from 120 raw images) of EB1–GFP and 4D–GFP. Scale bar: 0.5 µm. (D) The intensity profiles of comet signals along the longitudinal axis of microtubules. Black: EB1–GFP. Red: 4D–GFP. The integrated signal of this line profile was used for quantification of the intensity of EB1 comets, shown in E. (E) Statistical comparison of the integrated intensity of comet signals. EB1–GFP, *n*=3 assays (80 microtubules); 2D–GFP, *n*=3 assays (68 microtubules); 4D–GFP, *n*=3 assays (56 microtubules); S155D–GFP, *n*=3 assays (76 microtubules); T166D–GFP, *n*=3 assays (60 microtubules). Open symbols show means of independent assays, closed symbols show mean±s.d. of all assays. ***P*<0.01; ns, not significant; two-tailed Student's *t*-test. (F) The apparent association rates of EB1–GFP and the mutants (at a tubulin concentration of 16 µM). EB1–GFP, *n*=3 assays (101 microtubules); 2D–GFP, *n*=3 assays (152 microtubules); 4D–GFP, *n*=3 assays (234 microtubules); S155D–GFP, *n*=3 assays (94 microtubules); T166D–GFP, *n*=3 assays (93 microtubules). Open symbols show means of independent assays, closed symbols show mean±s.d. of all assays. **P*<0.05. ***P*<0.01; ns, not significant; two-tailed Student's *t*-test. Note that all five EB1 variants at the working concentration (5 nM) have negligible effects on microtubule growth velocity. (G) Probability distributions of the dwell time of single wild-type and mutant EB1–GFP molecules (EB1–GFP, *n*=253 events; 2D–GFP, *n*=128 events; 4D–GFP, *n*=78 events; S155D–GFP, *n*=136 events; T166D–GFP, *n*=148). The data were fitted to a single exponential function to calculate the dissociation rates (k_{off}). (H) The cumulative probability distributions of the dwell time of $EB1_{I224A}$–GFP (red; same data as shown in Fig. 2E) and 4D–GFP (blue) after a given period of time (Δt).

that increasing the concentration of phosphomimetic mutant EB1 could functionally compensate for the reduction in the binding affinity. Therefore, the weaker effects of phosphomimetic mutation of EB1 on microtubule dynamics could be accounted for by the weaker end-binding affinity of the mutant protein. Furthermore, we confirmed that non-GFP-tagged 4D showed significantly weaker binding to microtubules and weaker effects on microtubule dynamics in comparison to those shown by non-GFP-tagged EB1, similar to the differences observed between EB1–GFP and 4D–GFP (Fig. S3), which excluded potential interference with our findings by effects caused by the GFP-tag.

The 4D mutant can form a dimer, but with an altered structure

What could be the structural changes underlying the reduced end-binding affinity of the EB1 mutants? Because the binding kinetics of 4D–GFP are similar to those of the monomeric mutants, we checked whether dimerization is disrupted by the mutations. In size-exclusion chromatography experiments, all four mutants of EB1–GFP were eluted at the same position (Fig. 4A), suggesting no major changes in the overall shape and size of the proteins. Further single-molecule measurements showed that the fluorescence intensity of all the phosphomimetic mutants corresponded to a dimeric organization (Fig. 4B; Figs. S1, S2). Based on these results, we conclude that all four mutants form dimers.

Although the 4D–GFP mutant EB1 forms dimers, the end-binding affinity is close to that of a monomeric EB1–GFP, implying that the simultaneous binding of two monomers is probably hindered. What is the structural basis underlying this change in end-binding affinity? To answer this question, we used small-angle X-ray scattering (SAXS) to measure the molecular morphology of EB1, EB1–GFP, 4D and 4D–GFP (Fig. 4C). Based on the SAXS data, we calculated two parameters: the radius of gyration (R_g) and the maximum particle distance (D_{max}) (Table S1). 4D had a similar

Journal of Cell Science (2020) 133, jcs241216. doi:10.1242/jcs.241216

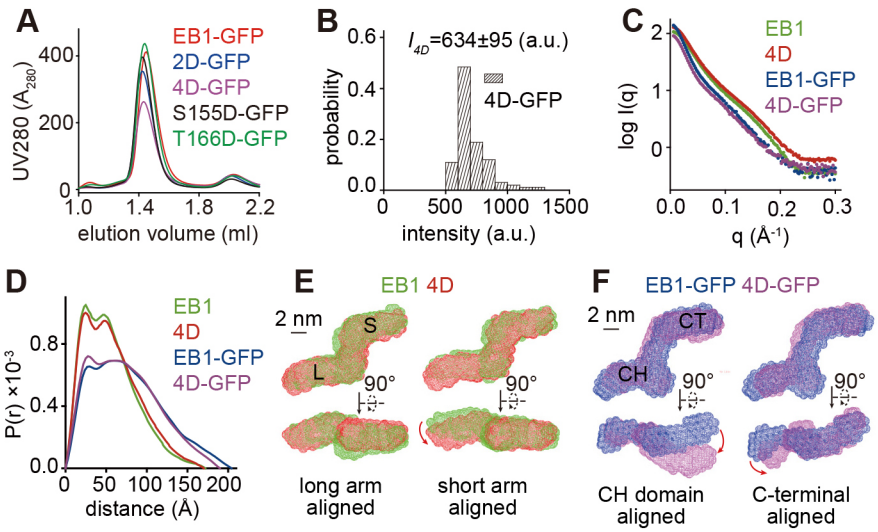

Fig. 4. The 4D mutant is dimeric but shows an altered structure. (A) Plots of A_{280} against elution volume from size-exclusion chromatograph experiments. Red, EB1–GFP; blue, 2D–GFP; pink, 4D–GFP; black, S155D–GFP; green, T166D–GFP. (B) Distribution of the fluorescence intensity of individual 4D–GFP binding events. The mean±s.d. intensity is shown (n=98 events). (C) Experimental SAXS scattering profiles of EB1 (green), 4D (red), EB1–GFP (blue) and 4D–GFP (purple). (D) PDDFs of EB1, 4D, EB1–GFP, and 4D–GFP, color coded as in C. (E) The overlay of the calculated SAXS envelopes of EB1 and 4D shown in two angles of view. Left, long arm aligned; right, short arm aligned. L: long arm. S: short arm. Scale bar: 2 nm. (F) The overlay of the calculated SAXS envelopes of EB1–GFP and 4D–GFP. Left, CH domain aligned; right, carboxyl-terminus (C-terminal) aligned. Scale bar: 2 nm.

R_g but a smaller D_{max} in comparison to EB1 (Table S1). The R_g and D_{max} of 4D–GFP were smaller than those of EB1–GFP. These results suggest a structural compaction in the presence of the phosphomimetic mutations. We then plotted the pair distance distribution function (PDDF) from the SAXS data, which represents the distribution of interatomic distances within a molecule. The PDDF of EB1 was characterized by two peaks, as previously reported (Buey et al., 2011). The first peak was interpreted as representing short interatomic distances (e.g. within the CH domain), and the second peak as representing long interatomic distances (e.g. between the CH and coiled-coil domains). In agreement with this, the addition of GFP to the carboxyl-terminus of EB1 shifted the second peak towards longer distances without altering the position of the first peak. The comparison between EB1 and 4D, as well as between EB1–GFP and 4D–GFP, showed that the 4D mutations did not change the two-peak pattern in the PDDF plot (Fig. 4D), suggesting that the structural change, if any, is local.

We then calculated the SAXS envelope, which characterizes the overall morphology of the molecules. The SAXS envelope of EB1 showed a zigzag shape with two arms of different lengths (the longer being ∼11 nm, the shorter ∼8 nm). The longer and shorter arms of EB1 were able to overlap fairly well with their counterparts in 4D. However, no matter which arm was used as the alignment reference for the entire EB1, the other arm could not overlap well with its counterpart, and showed an ∼20° deflection (Fig. 4E). This suggests that 4D adopted a more curved conformation compared to the conformation of EB1 (Fig. 4E). However, we were unable to distinguish the amino-terminus (CH domain) and the carboxyl-terminus (coiled-coil domain) of non-tagged EB1 and 4D using their SAXS envelopes. To solve this issue, we calculated the SAXS envelopes of wild-type EB1–GFP and 4D–GFP (Fig. 4F). The SAXS envelope for EB1–GFP also showed a zigzag shape. The longer arm had a length of ∼11 nm, similar to the longer arm of EB1. The shorter arm (∼10 nm long) was longer than the shorter arm of EB1, probably due to the addition of the GFP-tag at the carboxyl-terminus (Fig. 4F). When compared separately, both arms of EB1–GFP overlapped fairly well with their counterparts in 4D–GFP. However, when the carboxyl-terminus was used as the alignment reference, we found that in the SAXS envelope of 4D–GFP, the longer arm (corresponding to the CH domains) showed an ∼20° deflection relative to the longer arm of EB1–GFP (Fig. 4F), confirming that the 4D mutant adopts a more curved shape.

The 4D mutant shows altered intramolecular interactions

How does the structural change resulting from the 4D mutations lead to the reduction in end-binding affinity? To address this question, we analyzed the effects of the 4D mutations on the structure of the linker domain itself (local) and the entire EB1 dimer (global). To measure the local changes, we purified the linker domain of EB1 and 4D (amino acids 131–191; Fig. 3A) and analyzed their structures in solution using nuclear magnetic resonance (NMR) (Fig. 5A). Four parameters were measured: ^{15}N longitudinal spin relaxation rate (R_1), ^{15}N transverse spin relaxation rate (R_2), ^{1}H–^{15}N heteronuclear nuclear Overhauser effect (NOE) and chemical shift perturbation upon mutation ($\Delta\delta_{NH}$). Most of the resonances in heteronuclear single quantum coherence (HSQC) spectra of the two linker domain peptides were distributed in a narrow region (Fig. S4), indicating that they are both disordered. This conclusion is supported by the overall negative NOE values of the two peptides (Fig. 5A). The ^{15}N R_1, R_2 and ^{1}H–^{15}N heteronuclear NOE of the two peptides (Fig. 5A) were nearly identical in most residues, indicating that the overall flexibility of both peptides is similar. Despite these similarities, we noted some considerable local differences between the two peptides. For example, the increased R_2 rates at K21, L23, Q37 and T39 (Fig. 5A) and the increased NOEs at the four phosphomimetic mutation sites (Fig. 5A) suggest that the 4D linker has local structural compactness. Many of these residues were charged, or were adjacent to charged residues, implying that the compactness is likely due to altered electrostatic interactions. This result is further supported by the altered chemical shifts (Fig. 5A) around these mutation sites.

We then probed the global intramolecular organization of full-length EB1 and 4D by measuring the hydrogen/deuterium exchange (HDX) rate using mass spectrometry (Engen and Smith, 2000; Engen and Wales, 2015). HDX rate measures how exposed a peptide is to hydrogen/deuterium exchange in a protein molecule. Therefore, a change in the HDX rate could reflect whether this peptide adopts a more buried (a slower HDX rate) or more exposed (a faster HDX rate) conformation. In our HDX measurements of EB1, the peptides in the coiled-coil domain showed very low HDX rates, while those in the CH (microtubule-binding) and linker domains showed higher HDX rates (Fig. 5B), consistent with the known organization of EB1 (Akhmanova and Steinmetz, 2008). This overall pattern was not changed in 4D, consistent with 4D

Journal of Cell Science (2020) 133, jcs241216. doi:10.1242/jcs.241216

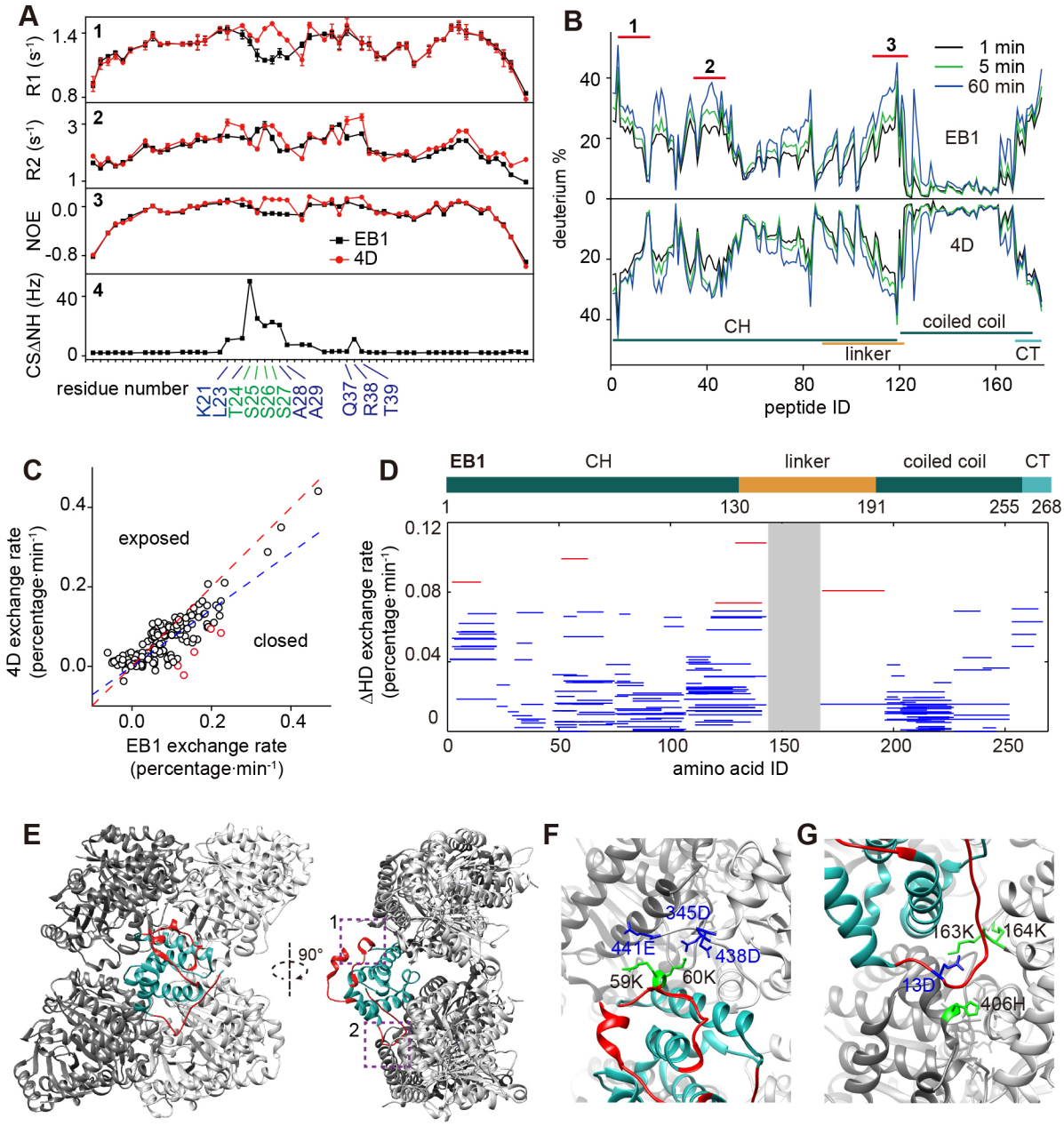

Fig. 5. The 4D mutant shows altered intramolecular interactions. (A) NMR analyses of the purified linker$_{wt}$ and linker$_{4D}$. (1) ^{15}N spin relaxation rate R1; (2) ^{15}N spin relaxation rate R2; (3) heteronuclear ^{1}H-^{15}N Nuclear Overhauser Effect; (4) chemical shift (CSΔNH) of linker$_{4D}$ relative to linker$_{wt}$. In 1–3, black line shows linker$_{wt}$, red line shows linker$_{4D}$. The residues showing local compactness are indicated at the bottom. (B) Plots showing the HDX of EB1 (upper panel) and 4D (lower panel) against time. Numbered bars indicate regions that show the most significant changes in the HDX rate between EB1 and 4D. The protein domains of EB1 are indicated (CT, C-terminal domain). (C) Plots of the HDX rates of all 4D peptides against those of their EB1 counterparts. Every circle represents one specific peptide. All points were fitted to a linear function (blue dashed line). The five peptides with the greatest changes in the exchange rate (top 3%) are shown as red circles. The red dashed line has a slope of 1 and passes through the origin. Note that the blue line has a smaller slope than the red one. (D) All peptides detected using mass spectrometry are mapped to the EB1 domain schematic and their differential HDX rates are shown on the *y*-axis. The five peptides with the largest changes in the exchange rate (top 3%) are shown in red. The gray box marks the region where the differential HDX rate cannot be measured due to the presence of the phosphomimetic mutations. (E) Cryo-EM structure of a single CH domain (cyan) of an EB protein (EB3, also known as MAPRE3) (Zhang et al., 2015) and four tubulin dimers from an atomic model of the GMPCPP-stabilized microtubule (α-tubulin, light gray; β-tubulin, dark gray; PDB ID 3JAL). The regions showing the greatest difference (top 3%) in HDX rate are indicated in red. Left panel: side view. Right panel: top view. The two dashed boxes indicated the regions that are enlarged in F and G. (F) The enlarged region indicated with box 1 in E. The positively charged residues (green) of EB1 and the negatively charged residues (blue) of tubulin are shown at the EB1–microtubule binding interface. (G) The enlarged region indicated with box 2 in E. The positively charged residues (green) in tubulin and negatively charged residues (blue) in EB1 are shown at the EB1–microtubule binding interface.

forming dimers. We then compared the HDX rates of 179 pairs of peptides (91% coverage) in EB1 and 4D. We plotted the HDX rates of all 4D peptides against those of their EB1 counterparts and fitted a linear function to the scattered points (blue dashed line in Fig. 5C). The slope of the fitted line was less than one (Fig. 5C), suggesting that many hydrogen/deuterium exchangeable sites in 4D tend to adopt a more buried conformation than in EB1. This agrees with the structural compaction observed in the SAXS data, and demonstrates

Journal of Cell Science

Journal of Cell Science (2020) 133, jcs241216. doi:10.1242/jcs.241216

that intramolecular interactions in 4D are altered. We picked 5 peptides whose HDX rates were most deviated from their counterparts in EB1 (representing the top 3% of all peptides; see Fig. S4 for the top 10%). These peptides mapped to three regions, with two located in the CH domain and one in the linker domain (Fig. 5D). The affected regions in the CH domain contained charged residues (Fig. S4), suggesting that the changes in the HDX rate are likely due to altered electrostatic intramolecular interactions in the 4D mutant. Furthermore, these peptides are located at binding interfaces (Fig. 5E–G) that have been proposed to mediate the EB1–microtubule interaction [for example amino acids 2–15 (Zhang et al., 2015) and residues K59 and K60 (Slep and Vale, 2007)]. Because the EB1–microtubule interaction is electrostatic (Zanic et al., 2009), conformational and electrostatic changes in the binding interfaces are expected to directly contribute to the reduction in the end-binding affinity of EB1. Taken together, these analyses provide structural insights into the low end-binding affinity of the 4D mutant.

DISCUSSION

A working model of EB1 high-affinity end binding

This study provides direct biochemical evidence for the idea that the dimeric organization of EB1 enhances its end-binding affinity by facilitating the binding of two CH domains to the growing end of dynamic microtubules (Fig. 6). In our proposed model, the linker domain is important for the overall architecture of EB1 and can be considered as an adjustable switch that tunes the end-binding affinity in response to phosphoregulation. When the linker domain is phosphorylated, EB1 dimers adopt a more curved conformation, in which the two CH domains in the dimer are structurally rearranged and CH domain–microtubule binding is electrostatically disrupted. In this scenario, EB1 converts to a low-affinity state (Fig. 6).

The key observations that support this model are that the EB1 mutant 4D, which carries phosphomimetic mutations in the linker domain, shows a reduced end-binding affinity and adopts a more curved conformation. As mentioned above, two possible mechanisms may account for the reduction in end-binding affinity.

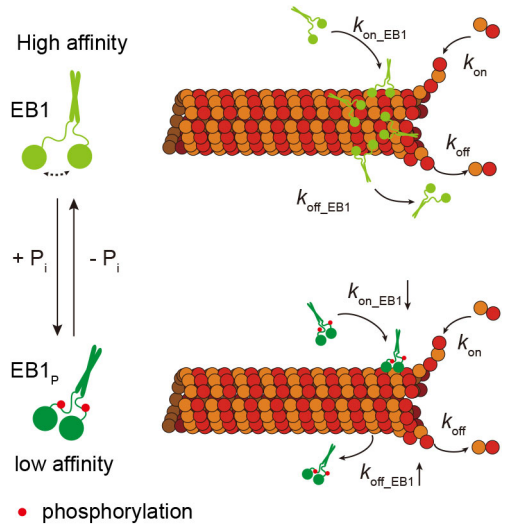

Fig. 6. Diagram depicting organization of the EB1 dimer and regulation of EB1 end-binding affinity by phosphorylation. Wild-type EB1 dimers show a high affinity to the growing end of microtubules. Upon phosphorylation on the linker domain, the EB1 dimers adopt a more curved conformation and convert into a low-affinity state (with a lower on-rate and a higher off-rate).

In the first, the linker domain is important for organization of the overall architecture of EB1, which is key for the high end-binding affinity. In this case, phosphorylation of the linker domain could change the intramolecular interactions of the EB1 dimer, altering the overall architecture of EB1 and in turn leading to a reduction in end-binding affinity. In the second possible mechanism, the linker domain could contribute to the binding affinity through direct electrostatic interactions with the microtubule lattice, in addition to the canonical microtubule–CH domain interaction. In this scenario, phosphorylation may interfere the linker–microtubule interaction, weakening the end-binding affinity of EB1. While we cannot absolutely exclude the second possibility, we propose that the first mechanism contributes to the high end-binding affinity of EB1. This is based on the following evidence. First, EB1 binds to microtubules with both CH domains of the dimer, so the two CH domains need to be properly spaced to fit the lattice structure of microtubules. Our results show that wild-type EB1 dissociates from microtubule ends with a smaller probability than that of two independent monomers, suggesting that the two monomers in the dimer are organized to facilitate the high end-binding affinity. The linker domain, thought to be responsible for the overall architecture of EB1, likely contributes to such an organization. Second, we show that the 4D mutant adopts a more curved conformation, which primarily affects the orientation of the microtubule-binding CH domains; an observation consistent with the overall architecture being crucial for end-binding affinity. Such an altered binding may disfavor the simultaneous binding of two CH domains, interfere with the reattachment of EB1 monomers within the dimer or weaken the CH–microtubule interactions (Fig. 5). This could account for the reduction of end-binding affinity in the 4D mutant to the level of monomeric EB1 mutants. Third, the monomeric mutant EB1$_{I224A}$–GFP has a similar binding kinetics to those of the truncated mutant EB1$_{143}$–GFP, suggesting that the linker domain, at least in its monomeric form, does not significantly increase the microtubule binding affinity of single CH domains. Finally, it should be noted the two candidate mechanisms are not necessarily exclusive.

Functional implications

Our data suggest that the intramolecular organization of EB1 promotes its end-binding affinity and is susceptible to phosphoregulation, suggesting a molecular mechanism to modulate the function of EB1. Such a mechanism has several advantages. First, it is reversible and can be coupled to other phosphoregulated events, which is important for the synchronization of multiple subcellular events during complicated cell physiological processes, such as mitosis. Second, phosphorylation is expected to electrostatically alter the way that the linker domain interacts with other domains without disrupting dimerization, which allows prompt and reversible affinity switching. Third, in the presence of cellular kinase activities that maintain the resting phosphorylation state of EB1, the end-binding of EB1 can be inhibited or enhanced, which would endow a bidirectional regulation on the activity of EB1. A similar mechanism may also apply to other types of modifications to EB1, such as acetylation (Xia et al., 2014). Therefore, this work provides insights into how the function of EB1 and the dynamics of +TIP networks can be regulated in cells.

Limitations

The primary limitation of this study is that, due to technical limitations, our structural data do not provide the atomic resolution needed to resolve the structure of full-length EB1. Therefore, three issues remain unresolved. First, how exactly does the linker domain

Journal of Cell Science (2020) 133, jcs241216. doi:10.1242/jcs.241216

interact with the other parts of the EB1 dimer, and how are these interactions changed upon phosphorylation? Second, how are the two CH domains structurally arranged in the dimer, for example, what is the interdistance and the relative orientation of the two domains? Third, how do the two CH domains of an EB1 dimer structurally fit into their binding sites on the microtubule lattice? If EB1 undergoes an induced fit upon binding, it is possible that the high-affinity binding may actually reflect how the EB1 dimer–microtubule interaction can be facilitated by the in-solution structure of EB1. To address these issues, it is essential to solve the in-solution and microtubule-bound structures of EB1 to atomic resolution. Despite these unresolved issues, our results provide insights that help understanding of EB1 end-binding activity, and that are useful for future analyses.

MATERIALS AND METHODS

Tubulin purification and labeling

Crude tubulin was obtained from porcine brain through double cycles of polymerization and depolymerisation, as previously described (Gell et al., 2011). Tubulin was further purified using a TOG-based affinity column (Widlund et al., 2012). Tubulin was labeled with biotin (Thermo Fisher Scientific, 20217), TAMRA (Thermo Fisher Scientific, C1171) and Alexa Fluor 647 (Thermo Fisher Scientific, A20106) using NHS esters, following standard protocols (Hyman et al., 1991).

EB1 purification

Recombinant EB1 and the phosphomimetic mutants were expressed in the *BL21 E. coli* strain and purified using Ni Sepharose columns (QIAGEN, 30210). The cell lysis buffer used was 50 mM Na_2HPO_4–HCl, 300 mM KCl, 10% glycerol, 10 mM imidazole, 1 mM DTT, 0.1% Tween 20, pH 7.5. The column was washed with washing buffer (50 mM Na_2HPO_4–HCl, 300 mM KCl, 10% glycerol, 30 mM imidazole, 1 mM DTT, pH 7.5) and then balanced with the working buffer of 3C protease (50 mM Na_2HPO_4–HCl, 300 mM KCl, 10% glycerol, 10 mM imidazole, 1 mM DTT, pH 7.5). His-tags were removed using 3C protease (final concentration 6 µg/ml; Thermo Fisher Scientific, 88946) digestion on the Ni Sepharose column overnight (4°C), before the cleaved protein in 3C protease buffer was collected. Western blotting was performed using an anti-His antibody (see western blotting section) to verify the cleavage of His-tags. All purified proteins were kept in storage buffer until use [100 mM KCl, 10% glycerol and 1 mM DTT in 1×BRB80 (80 mM Pipes pH 6.9, 1 mM $MgCl_2$, and 1 mM EGTA)].

Western blotting

Protein samples were subjected to SDS–PAGE using a 10% Bis-Tris gel (Life Technologies, NP0301BOX) and transferred onto PVDF membrane (Millipore, ISEQ00010). The PVDF membrane was blocked using 1% non-fat milk in PBST (0.1% Tween 20 in 1× PBS) and incubated with an HRP-conjugated anti-His antibody at 1:3000 dilution in 1% non-fat milk in PBST. (CWBIO, 0285M). Antibody binding was detected using an eECL western blot kit (CWBIO, CW0049S).

Size-exclusion chromatography

A micro Superdex 200 increase column (GE, 28-9909-45) was first equilibrated in 1×BRB80 with 10% glycerol, 100 mM KCl and 1 mM DTT. Approximately 100 µl of purified protein sample (at about 1 mg/ml) was injected into the column and A280 was recorded during the elution process.

Microtubule dynamic assay

The microtubule dynamic assay was performed as described previously (Gell et al., 2010). Briefly, short GMPCPP-stabilized (Roche, NU-405L) microtubules (5% Alexa Fluor 647 labeled and 20% biotin labeled) were immobilized on the surface of a cover glass coated with a biotin-binding protein (Thermo Fisher Scientific, 31000). Free tubulin dimer (13% TAMRA labeled) was then added into the flow cell in imaging buffer (BRB80 supplemented with 2 mM GTP, 50 mM KCl, 0.15% sodium carboxymethylcellulose, 80 mM D-glucose, 0.4 mg/ml glucose oxidase, 0.2 mg/ml catalase, 0.8 mg/ml casein, 1% β-mercaptoethanol, 0.001% Tween 20). The growth of microtubules was recorded using a total internal reflection (TIRF) microscope (Olympus) equipped with an Andor 897 Ultra EMCCD camera (Andor, Belfast, UK) using a 100× TIRF objective (NA 1.49; Olympus). To record microtubule dynamics, images were taken every second with a 0.1 s exposure. To record single-molecule binding of EB1, the concentration of KCl in the imaging buffer was increased to 100 mM in order to reduce the formation of EB1 aggregates. Images were taken every 0.1 s with a 0.05 s exposure.

Image analysis

Microtubule growth rate and catastrophe frequency were measured using Fiji, as described previously (Feng et al., 2017; Schindelin et al., 2012).

Single-molecule measurement using TIRF

Single molecules of EB1–GFP at the growing end of microtubules were recorded in the presence of free tubulin dimers and 5 nM EB1–GFP. By measuring the intensity of background noise, monomeric EB1–GFP ($EB1_{143}$) and dimeric EB1–GFP (Fig. S1), we confirmed that the fluorescence intensity of a single EB1–GFP dimer is 665±139 (a.u.). Using this as a standard, we then measured the number of binding events and the dwell time of each single-molecule binding event. The association rate (k_{on}) was estimated by counting the number of EB1–GFP binding events per microtubule tip per unit time (5 nM protein). The dissociation rate (k_{off}) of EB1–GFP was calculated by fitting the distribution of the dwell time of EB1 molecules with a single exponential function.

Microtubule end tracking and image averaging

Microtubule ends were tracked as previously described (Maurer et al., 2014). Briefly, a two-dimensional model that describes the microtubule lattice as a Gaussian wall, and its end as a half-Gaussian, was used to fit the areas in the raw images where microtubules were identified, allowing the position of the microtubule ends in every frame to be determined. The position of microtubule ends was used as a reference for aligning and averaging the EB1–GFP comet signals in the time-series movies. The intensity profile of the averaged EB1–GFP signal along the direction of microtubule growth was fitted to an exponentially modified Gaussian function. The integrated EB1–GFP signal was used to quantify the total intensity of the EB1–GFP signal at the microtubule growing end.

Tracking the position of individual EB1–GFP molecules at microtubule ends

To measure the position of individual EB1–GFP molecules at microtubule ends, a Gaussian function was used to fit the intensity profile of individual EB1–GFP molecules. The peak location (relative to the position of the microtubule end) was recorded as the position of each EB1–GFP. The positional distribution of EB1–GFP binding sites was plotted along the longitudinal axis of microtubules and fitted to an exponentially modified Gaussian function to calculate the FWHM as an estimation of the length of the EB1 binding region.

Microtubule pulldown assay

GMPCPP-stabilized microtubules (0.2 mg tubulin) were polymerized and resuspended in 1×BRB80 (100 µl). A mixture of microtubules and protein (20 µl warm 1×BRB80, 20 µl microtubules and 10 µl protein samples at 2.5 mg/ml) was incubated at 37°C for 5 min and then spun down using an Air-Driven Ultracentrifuge (BECKMAN, 340401). The supernatants were saved and the pellets were resuspended in ice-cold 1×BRB80. Finally, the supernatants and pellets were analyzed using SDS–PAGE (Fig. S3).

SAXS

We performed SAXS on four EB1 variants (EB1, 4D, EB1–GFP and 4D–GFP) in the same buffer (100 mM KCl, 10% glycerol and 1 mM DTT in 1×BRB80). The stock concentration of all protein samples was 4 mg/ml. SAXS measurements were carried out at room temperature at the beamline BL19U2 of the National Center for Protein Science in Shanghai and

Shanghai Synchrotron Radiation Facility (Table S2). The scattered X-ray photons were recorded using a PILATUS 100k detector (Dectris, Switzerland). Detection settings were adjusted to obtain the scattering q between 0.009 $Å^{-1}$ and 0.415 $Å^{-1}$, where $q=(4\pi/\lambda)\cdot\sin\theta$ and 2θ is the scattering angle. A total of 20 2D images were recorded for each sample using a flow cell. An exposure of 0.5–2.0 s was used in order to minimize radiation damage and obtain a good signal-to-noise ratio. The absence of systematic signal changes in sequentially collected X-ray scattering images confirmed that there was no radiation damage in our experiments.

The 2D images were then reduced to 1D scattering profiles using BioXTAS Raw (Hopkins et al., 2017). Scattering profiles were calculated by subtracting the background buffer contribution from the sample–buffer profile using the program PRIMUS following standard procedures (Konarev et al., 2003; Wang et al., 2009). Concentration series measurements (4- and 2-fold dilution series) were carried out for each protein to remove the scattering contribution due to inter-particle interactions and to extrapolate the data to infinite dilution. The forward scattering intensity $I(0)$ and the radius of gyration (R_g) were calculated from the data of infinite dilution at the low q values in the range of $q\cdot R_g<1.3$, using the Guinier approximation: $\ln(I(q)) \approx \ln(I(0)) - R_g^2\cdot q^2/3$. $I(0)$ and R_g can also be estimated from the scattering profiles with a broader q range of 0.006-0.30 $Å^{-1}$ using the indirect Fourier transform method implemented in the program GNOM (Svergun, 1992), along with the pair distance distribution function [PDDF, $p(r)$], and the maximum dimension of the protein, D_{max}. The molecular weights of solutes were calculated on a relative scale using the R_g/V_c power law developed by Rambo and Tainer (2013). The theoretical scattering intensity of the atomic structure model was calculated and fitted to the experimental scattering intensity using CRYSOL (Svergun et al., 1995).

The low-resolution envelopes of proteins were modeled *ab initio* using a simulated annealing algorithm, implemented in the program DAMMIN (Svergun, 1999). Twenty independent runs were performed, and the resulting models were subjected to averaging by DAMAVER (Volkov and Svergun, 2003). In this program, the normalized spatial discrepancy (NSD) between each pair of models was computed. NSD provides a quantitative measure for the similarity between two models. If two models systematically differ from each other the NSD exceeds 1, for identical objects it is 0. The models that met the NSD criteria ($NSD < NSD_{mean}+2\times NSD_{s.d.}$, NSD_{mean}, mean value of NSD of each model; $NSD_{s.d.}$, standard deviation of NSD of each model) were superimposed onto the reference model (with the lowest NSD compared to the rest of the models) using SUPCOMB (Kozin and Svergun, 2001). The final model was obtained after DAMFILT filtering (Volkov and Svergun, 2003).

HDX assay

For our HDX reaction, 5 µl protein samples (2 mg/ml) in protein sample buffer (100 mM KCl, 10% glycerol and 1 mM DTT in 1×BRB80) were diluted with 45 µl D_2O-based buffer (protein sample buffer with H_2O replaced by D_2O). The diluted protein samples were incubated at 10°C for 1 min, 5 min and 60 min. HDX was quenched by adding 50 µl quenching buffer (4 M guanidine hydrochloride, 0.1 M TCEP and 0.2 M citric acid). Pepsin was used to digest the proteins on ice for 5 min. The digested samples were then centrifuged (16,000 ***g***, 12,000 rpm) at 4°C for 1 min, and the supernatant collected for liquid chromatography-tandem mass spectrometry (LC-MS/MS) analysis. In the LC-MS/MS analysis, peptides were separated by a 40 min gradient elution at a flow rate of 0.100 ml/min at 0°C using a Thermo-Dionex Ultimate 3000 RS pump HPLC system (Thermo Fisher Scientific), which was directly interfaced with a Thermo Scientific Q Exactive hybrid quadrupole-Orbitrap mass spectrometer (Thermo Fisher Scientific). The analytical column was an ACQUITY UPLC BEH C18 1.7 µm column (2.1×50 mm length; Waters). Mobile phase A consisted of 0.1% formic acid, and mobile phase B consisted of 100% acetonitrile and 0.1% formic acid. An Orbitrap mass spectrometer (Thermo Fisher Scientific) was operated in data-dependent acquisition mode using Xcalibur 4.0 software (Thermo Fisher Scientific). There was a single full-scan mass spectrum in the Orbitrap (350–2000 *m/z*, 70,000 resolution) followed by 10 data-dependent MS/MS scans in the Orbitrap (17,500 resolution) at 30% normalized collision energy (HCD). The MS/MS spectra from each LC-MS/MS run were searched against the sequences of EB1 and 4D using an in-house Proteome Discovery (Ver 1.4, Thermo, US) searching algorithm. HDX/MS data analysis was performed using HDExaminer (Ver 2.3.0, Sierra Analytics, CA).

Linker domain preparation for NMR analysis

The coding sequences of $linker_{eb1}$ and $linker_{4D}$ were cloned into the pET28a-SUMO vector (Tiandz, 60908-2831) by homologous recombination, and then transformed into BL21-Gold (DE3) *E. coli* strain (Solarbio, C1400). M9 medium (Li et al., 2002) was used to express uniformly ^{15}N-labeled or $^{15}N/^{13}C$-labeled proteins using ^{15}N-ammonium chloride and ^{13}C-glucose as the sole nitrogen and carbon sources. Bacteria were inoculated in 10 ml starter LB cultures overnight and then transferred to M9 media in which bacteria were grown at 37°C until the OD_{600} reached ∼0.6–0.8. Protein expression was induced by addition of 0.5 mM IPTG. Bacteria were then collected in 50 ml buffer (500 mM NaCl, 10 mM imidazole, 20 mM Tris–HCl, pH 8.0) and lysed using a high-pressure homogenizer. Proteins were purified using a Ni Sepharose column (GE, 17-5247-01) and the SUMO tag was cleaved by Ulp1 protease (Solarbio, P2070). The purified protein samples were exchanged into NMR buffer (50 mM sodium chloride, 20 mM phosphate, pH 6.0) using 3 kDa-cutoff Amicon centrifugal filter units (Millipore). The purity of proteins was confirmed to be >95% by SDS−PAGE. Sample concentrations were measured by UV absorption at 215 nm due to the lack of aromatic residues in the purified proteins. Each sample was supplied with 8% D_2O to enable NMR measurement.

NMR measurement and data processing

Two ^{15}N labeled $linker_{wt}$ and $linker_{4D}$ samples with concentrations of 500 µM were used for measurement of ^{1}H-^{15}N heteronuclear single quantum coherence (HSQC), ^{15}N R_1, ^{15}N R_2, and heteronuclear ^{1}H-^{15}N NOE. Another two $^{15}N/^{13}C$-labeled $linker_{wt}$ and $linker_{eb1}$ samples with concentrations of ∼1 mM were used for backbone assignments. To this end, a set of standard triple-resonance experiments were conducted, including CBCAcoNH, HNCACB, HNCO and HNcaCO (Grzesiek and Bax, 1992). Finally, 46 residues in $linker_{wt}$ and 47 residues in $linker_{eb1}$ were assigned. The unassigned residues were either prolines or residues that suffered from severe peak overlap. All NMR data were collected at 25°C using a Bruker Avance DRX 800 MHz spectrometer equipped with a TCI cryoprobe. The ^{15}N R_2, ^{15}N R_1, and NOE data were processed using nmrPipe (Delaglio et al., 1995) and Sparky (T. D. Goddard and D. G. Kneller, SPARKY 3, University of California, San Francisco; https://www.cgl.ucsf.edu/home/sparky/). Peak volumes were obtained using the autoFit script of NMRPipe. The R_1 and R_2 values were calculated by fitting peak volumes at different time delays to a mono-exponential function. Errors were estimated using a Monte Carlo-based approach with 100 iterations.

Acknowledgements

The authors thank all members of the Liang laboratory for discussions, reading of this article and feedback. We thank the protein chemistry facility (mass spectrometry) and cell biology facility (TIRF microscope) at the Center for Biomedical Analysis of Tsinghua University. We thank Dr Ning Xu at the NMR facility of the China National Center for Protein Sciences, Beijing, for his technical assistance.

Competing interests

The authors declare no competing or financial interests.

Author contributions

Conceptualization: X.L.; Methodology: Y.S., Y.Z., Y.P., J.H., Y.W., W.C., J.G., H.D., Y.X., X.F.; Formal analysis: Y.S., Y.Z., Y.P., J.H., Y.W., W.C., J.G., H.D., Y.X., X.F., X.L.; Investigation: Y.S., Y.Z., Y.P., J.H., Y.W., W.C., J.G., H.D., Y.X., X.F., X.L.; Writing - original draft: Y.S., X.L.; Supervision: X.L.; Project administration: X.L.; Funding acquisition: X.L.

Funding

We acknowledge our funding from Nation Key R&D Program of China (Ministry of Science and Technology of the People's Republic of China (2017YFA0503502), National Natural Science Foundation of China (31922018) and Qingdao National Laboratory for Marine Science and Technology (QNLM2016ORP0301). X.L. was supported by the Max-Planck Partner Group Program and Tsinghua-Peking Joint Center for Life Sciences.

Data availability

Experimental data of ^{1}H, ^{15}N, and ^{13}C chemical shifts and the R1, R2, and $^{15}N\{^{1}H\}$ NOE for protein backbone amides have been deposited in the Biological Magnetic Resonance Data Bank database (http://www.bmrb.wisc.edu) under accession numbers BMRB-50119 and BMRB-50120 for the wild-type and 4D mutant linker domains, respectively.

Supplementary information

Supplementary information available online at
http://jcs.biologists.org/lookup/doi/10.1242/jcs.241216.supplemental

Peer review history

The peer review history is available online at https://jcs.biologists.org/lookup/doi/10.1242/jcs.241216.reviewer-comments.pdf

References

Akhmanova, A. and Steinmetz, M. O. (2008). Tracking the ends: a dynamic protein network controls the fate of microtubule tips. *Nat. Rev. Mol. Cell Biol.* **9**, 309-322. doi:10.1038/nrm2369

Bowne-Anderson, H., Zanic, M., Kauer, M. and Howard, J. (2013). Microtubule dynamic instability: a new model with coupled GTP hydrolysis and multistep catastrophe. *BioEssays* **35**, 452-461. doi:10.1002/bies.201200131

Bowne-Anderson, H., Hibbel, A. and Howard, J. (2015). Regulation of microtubule growth and catastrophe: unifying theory and experiment. *Trends Cell Biol.* **25**, 769-779. doi:10.1016/j.tcb.2015.08.009

Buey, R. M., Mohan, R., Leslie, K., Walzthoeni, T., Missimer, J. H., Menzel, A., Bjelić, S., Bargsten, K., Grigoriev, I., Smal, I. et al. (2011). Insights into EB1 structure and the role of its C-terminal domain for discriminating microtubule tips from the lattice. *Mol. Biol. Cell* **22**, 2912-2923. doi:10.1091/mbc.e11-01-0017

Delaglio, F., Grzesiek, S., Vuister, G. W., Zhu, G., Pfeifer, J. and Bax, A. (1995). NMRPipe: a multidimensional spectral processing system based on UNIX pipes. *J. Biomol. NMR* **6**, 277-293. doi:10.1007/BF00197809

Dixit, R., Barnett, B., Lazarus, J. E., Tokito, M., Goldman, Y. E. and Holzbaur, E. L. F. (2009). Microtubule plus-end tracking by CLIP-170 requires EB1. *Proc. Natl. Acad. Sci. USA* **106**, 492-497. doi:10.1073/pnas.0807614106

Duellberg, C., Cade, N. I., Holmes, D. and Surrey, T. (2016). The size of the EB cap determines instantaneous microtubule stability. *eLife* **5**, e13470. doi:10.7554/eLife.13470

Engen, J. R. and Smith, D. L. (2000). Investigating the higher order structure of proteins. In *Mass Spectrometry of Proteins and Peptides: Mass Spectrometry of Proteins and Peptides* (ed. J. R. Chapman), pp. 95-112. Totowa, NJ: Humana Press.

Engen, J. R. and Wales, T. E. (2015). Analytical aspects of hydrogen exchange mass spectrometry. *Annu. Rev. Anal. Chem.* **8**, 127-148. doi:10.1146/annurev-anchem-062011-143113

Feng, S., Song, Y., Shen, M., Xie, S., Li, W., Lu, Y., Yang, Y., Ou, G., Zhou, J., Wang, F. et al. (2017). Microtubule-binding protein FOR20 promotes microtubule depolymerization and cell migration. *Cell Discov.* **3**, 17032. doi:10.1038/celldisc.2017.32

Feng, Q., Mickolajczyk, K. J., Chen, G.-Y. and Hancock, W. O. (2018). Motor reattachment kinetics play a dominant role in multimotor-driven cargo transport. *Biophys. J.* **114**, 400-409. doi:10.1016/j.bpj.2017.11.016

Galjart, N. (2010). Plus-end-tracking proteins and their interactions at microtubule ends. *Curr. Biol.* **20**, R528-R537. doi:10.1016/j.cub.2010.05.022

Gardner, M. K., Charlebois, B. D., Jánosi, I. M., Howard, J., Hunt, A. J. and Odde, D. J. (2011). Rapid microtubule self-assembly kinetics. *Cell* **146**, 582-592. doi:10.1016/j.cell.2011.06.053

Gell, C., Bormuth, V., Brouhard, G. J., Cohen, D. N., Diez, S., Friel, C. T., Helenius, J., Nitzsche, B., Petzold, H., Ribbe, J. et al. (2010). Microtubule dynamics reconstituted in vitro and imaged by single-molecule fluorescence microscopy. **95**, 221-245. doi:10.1016/S0091-679X(10)95013-9

Gell, C., Friel, C. T., Borgonovo, B., Drechsel, D. N., Hyman, A. A. and Howard, J. (2011). Purification of tubulin from porcine brain. In *Microtubule Dynamics: Methods and Protocols* (ed. A. Straube), pp. 15-28. Totowa, NJ: Humana Press.

Grzesiek, S. and Bax, A. (1992). An efficient experiment for sequential backbone assignment of medium sized isotopically enriched proteins. *J. Magn. Reson.* **99**, 201-207.

Hopkins, J. B., Gillilan, R. E. and Skou, S. (2017). BioXTAS RAW: improvements to a free open-source program for small-angle X-ray scattering data reduction and analysis. *J. Appl. Crystallogr.* **50**, 1545-1553. doi:10.1107/S1600576717011438

Howard, J. (2001). *Mechanics of Motor Proteins and the Cytoskeleton*: Sinauer Associates, Publishers.

Hyman, A., Drechsel, D., Kellogg, D., Salser, S., Sawin, K., Steffen, P., Wordeman, L. and Mitchison, T. (1991). [39] Preparation of modified tubulins. *Methods Enzymol.* **196**, 478-485. doi:10.1016/0076-6879(91)96041-O

Komarova, Y., De Groot, C. O., Grigoriev, I., Gouveia, S. M., Munteanu, E. L., Schober, J. M., Honnappa, S., Buey, R. M., Hoogenraad, C. C., Dogterom, M. et al. (2009). Mammalian end binding proteins control persistent microtubule growth. *J. Cell Biol.* **184**, 691-706. doi:10.1083/jcb.200807179

Konarev, P. V., Volkov, V. V., Sokolova, A. V., Koch, M. H. J. and Svergun, D. I. (2003). PRIMUS: a windows PC-based system for small-angle scattering data analysis. *J. Appl. Crystallogr.* **36**, 1277-1282. doi:10.1107/S0021889803012779

Kozin, M. B. and Svergun, D. I. (2001). Automated matching of high- and low-resolution structural models. *J. Appl. Crystallogr.* **34**, 33-41. doi:10.1107/S0021889800014126

Li, M. X., Corson, D. C. and Sykes, B. D. (2002) Structure Determination by NMR. In: Vogel, H. J. (eds) Calcium-Binding Protein Protocols: Volume 2: Methods and Techniques. Methods in Molecular Biology, vol 173. Springer, Totowa, NJ.

Luo, Y., Ran, J., Xie, S., Yang, Y., Chen, J., Li, S., Shui, W., Li, D., Liu, M. and Zhou, J. (2016). ASK1 controls spindle orientation and positioning by phosphorylating EB1 and stabilizing astral microtubules. *Cell Discov.* **2**, 16033. doi:10.1038/celldisc.2016.33

Maurer, S. P., Bieling, P., Cope, J., Hoenger, A. and Surrey, T. (2011). GTPgammaS microtubules mimic the growing microtubule end structure recognized by end-binding proteins (EBs). *Proc. Natl. Acad. Sci. USA* **108**, 3988-3993. doi:10.1073/pnas.1014758108

Maurer, S. P., Fourniol, F. J., Bohner, G., Moores, C. A. and Surrey, T. (2012). EBs recognize a nucleotide-dependent structural cap at growing microtubule ends. *Cell* **149**, 371-382. doi:10.1016/j.cell.2012.02.049

Maurer, S. P., Cade, N. I., Bohner, G., Gustafsson, N., Boutant, E. and Surrey, T. (2014). EB1 accelerates two conformational transitions important for microtubule maturation and dynamics. *Curr. Biol.* **24**, 372-384. doi:10.1016/j.cub.2013.12.042

Nehlig, A., Molina, A., Rodrigues-Ferreira, S., Honoré, S. and Nahmias, C. (2017). Regulation of end-binding protein EB1 in the control of microtubule dynamics. *Cell. Mol. Life Sci.* **74**, 2381-2393. doi:10.1007/s00018-017-2476-2

Rambo, R. P. and Tainer, J. A. (2013). Accurate assessment of mass, models and resolution by small-angle scattering. *Nature* **496**, 477-481. doi:10.1038/nature12070

Reid, T. A., Coombes, C., Mukherjee, S., Goldblum, R. R., White, K., Parmar, S., McClellan, M., Zanic, M., Courtemanche, N. and Gardner, M. K. (2019). Structural state recognition facilitates tip tracking of EB1 at growing microtubule ends. *eLife* **8**, e48117. doi:10.7554/eLife.48117

Schindelin, J., Arganda-Carreras, I., Frise, E., Kaynig, V., Longair, M., Pietzsch, T., Preibisch, S., Rueden, C., Saalfeld, S., Schmid, B. et al. (2012). Fiji: an open-source platform for biological-image analysis. *Nat. Methods* **9**, 676-682. doi:10.1038/nmeth.2019

Slep, K. C. and Vale, R. D. (2007). Structural basis of microtubule plus end tracking by XMAP215, CLIP-170, and EB1. *Mol. Cell* **27**, 976-991. doi:10.1016/j.molcel.2007.07.023

Slep, K. C., Rogers, S. L., Elliott, S. L., Ohkura, H., Kolodziej, P. A. and Vale, R. D. (2005). Structural determinants for EB1-mediated recruitment of APC and spectraplakins to the microtubule plus end. *J. Cell Biol.* **168**, 587-598. doi:10.1083/jcb.200410114

Svergun, D. I. (1992). Determination of the regularization parameter in indirect-transform methods using perceptual criteria. *J. Appl. Crystallogr.* **25**, 495-503. doi:10.1107/S0021889892001663

Svergun, D. I. (1999). Restoring low resolution structure of biological macromolecules from solution scattering using simulated annealing. *Biophys. J.* **76**, 2879-2886. doi:10.1016/S0006-3495(99)77443-6

Svergun, D., Barberato, C. and Koch, M. H. J. (1995). CRYSOL - a program to evaluate x-ray solution scattering of biological macromolecules from atomic coordinates. *J. Appl. Crystallogr.* **28**, 768-773. doi:10.1107/S0021889895007047

Volkov, V. V. and Svergun, D. I. (2003). Uniqueness of ab initio shape determination in small-angle scattering. *J. Appl. Crystallogr.* **36**, 860-864. doi:10.1107/S0021889803000268

Wang, J., Zuo, X., Yu, P., Xu, H., Starich, M. R., Tiede, D. M., Shapiro, B. A., Schwieters, C. D. and Wang, Y.-X. (2009). A method for helical RNA global structure determination in solution using small-angle x-ray scattering and NMR measurements. *J. Mol. Biol.* **393**, 717-734. doi:10.1016/j.jmb.2009.08.001

Widlund, P. O., Podolski, M., Reber, S., Alper, J., Storch, M., Hyman, A. A., Howard, J. and Drechsel, D. N. (2012). One-step purification of assembly-competent tubulin from diverse eukaryotic sources. *Mol. Biol. Cell* **23**, 4393-4401. doi:10.1091/mbc.e12-06-0444

Xia, P., Liu, X., Wu, B., Zhang, S., Song, X., Yao, P. Y., Lippincott-Schwartz, J. and Yao, X. (2014). Superresolution imaging reveals structural features of EB1 in microtubule plus-end tracking. *Mol. Biol. Cell* **25**, 4166-4173. doi:10.1091/mbc.e14-06-1133

Zanic, M., Stear, J. H., Hyman, A. A. and Howard, J. (2009). EB1 recognizes the nucleotide state of tubulin in the microtubule lattice. *PLoS ONE* **4**, e7585. doi:10.1371/journal.pone.0007585

Zhang, R., Alushin, G. M., Brown, A. and Nogales, E. (2015). Mechanistic origin of microtubule dynamic instability and its modulation by EB proteins. *Cell* **162**, 849-859. doi:10.1016/j.cell.2015.07.012

Zimniak, T., Stengl, K., Mechtler, K. and Westermann, S. (2009). Phosphoregulation of the budding yeast EB1 homologue Bim1p by Aurora/Ipl1p. *J. Cell Biol.* **186**, 379-391. doi:10.1083/jcb.200901036